CHAPTER 5

Terbium Acylpyrazolone complexes: Synthesis, Structural Features, Fluorescence and Electronic properties.

5.1 Introduction

Terbium is significant among the lanthanides as it is crucial in fluorescent lamps [1], contributing to their efficiency and colour quality [2]. It is utilized in fluorescent lamps due to its role in phosphor production, emitting green light [3]. It is also used in nuclear applications, with certain isotopes being radioactive and employed in nuclear technologies and medical imaging [4]. Terbium's unique electronic and optical properties make it valuable in specific electronic devices and optical materials. It has limited reactivity, slowly reacting with water and soluble in acids, and forms a protective oxide layer in air [5]. This silvery-white, malleable metal is also known for its use in strong permanent magnets, particularly terbium cobalt magnets, in electronic and medical applications [6]. While it lacks a known biological role, it is crucial in specific technological and industrial applications [7].

Research on terbium complexes encompasses investigating coordination compounds formed by terbium ions with diverse ligands. This field explores the luminescent properties of terbium, especially in the green and blue spectra, for potential applications in lighting, displays, and optoelectronics [8,9]. Ligand design influences properties such as luminescence intensity and stability [10]. Additionally, terbium complexes are studied for sensing applications, with potential uses in chemical and biosensors [11]. Medical imaging applications, catalytic properties, magnetic behaviour, theoretical studies, and environmental monitoring are also focus areas within this interdisciplinary research domain [12,13].

Green emission in terbium complexes is crucial for its applications in diverse fields [14–16]. This feature allows for colour tuning, facilitating the creation of full-colour displays and lighting. The availability of green and blue light expands the range of the electromagnetic spectrum covered by terbium complexes, contributing to improved sensing and imaging applications [11]. In biological and medical imaging, green-emitting terbium complexes serve as contrast agents, providing new opportunities for molecular-level visualization [17,18]. The green-to-blue intensity ratio in terbium complexes is pivotal for various applications, particularly luminescence and optoelectronics [19,20]. This ratio plays a crucial role in colour tuning for displays, lighting, and visual signalling, contributing to the development of vibrant and full-colour displays. Terbium complexes with controlled ratios are integral to the design of optoelectronic devices like LEDs and lasers, influencing their overall performance

[19,20]. Optimizing the green-to-blue intensity ratio contributes to the efficiency of energy transfer processes within terbium complexes, impacting their performance in lighting and sensing applications [21]. Studying and manipulating this ratio provides insights into the photophysical properties of terbium complexes, aiding in the development of materials for diverse technological and scientific applications.

Acylpyrazolone ligands are recognized for their significant involvement in enhancing the absorption and luminescence efficiency of terbium complexes [22–24]. These ligands play a crucial role in sensitizing excitation and efficiently transferring energy to terbium ions, resulting in improved absorption properties, increased molar absorptivity, and enhanced luminescence, particularly in the visible spectrum [22]. The stability provided by acylpyrazolones to terbium complexes is vital for maintaining desired optical properties over time. Additionally, their structural flexibility allows for tunable properties, optimizing absorption and luminescence characteristics based on specific application requirements [22]. Hence, this Chapter involves the synthesis, crystal features, photophysical characteristics, and examination of the green-to-blue intensity ratio for three terbium complexes with acylpyrazolone ligands.

5.2 Experimental section

5.2.1 Chemical provisions

All three ligands [(3,5-dimethylphenyl)(5-hydroxy 1-(phenyl = **HL^4** / 3-chlorophenyl = **HL^5** / p-tolyl = **HL^6**) -1H-pyrazol-4-yl)methanone] were directly prepared and used as described in Chapter 2(a). Hydrated 99.9% pure terbium (III) chloride was purchased from Central Drug House (CDH) (P) Ltd.

5.2.2 Complex synthesis

An eight-coordinated terbium complex can be synthesized by refluxing an equimolar mixture of the ligand and NaOH (0.12 g, 3 mmol) with ethanolic terbium(III) chloride solution (1 mmol, 0.283 g) added dropwise for 18 hours, as illustrated in Figure 5.1. Upon gradual evaporation of the solvent, the complex product precipitates, while terbium(III) chloride remains in the supernatant.

Synthesis of complex 18

Complex $[Tb(L^4)_3(H_2O)_2]$ (**18**) was prepared using 3 eq HL^4 ligand (3 mmol, 0.92 g). Yield (%): 90.19% (1.0011 g), M.P.: >200 °C, Formula: $C_{57}H_{55}N_6O_8Tb$,

Formula wt: 1111.03. Elemental analysis: C, 61.62; H, 4.99; N, 7.56%; Found: C, 63.60; H, 5.167; N, 7.87%. Λ_M = 3.91 $\Omega^{-1}cm^2mol^{-1}$. **FTIR (KBr, cm^{-1}):** 2900-3100 (w, $\upsilon_{O\text{-}H\ water}$), 1617 (s, $\upsilon_{C=O\ DMB}$), 1596 (s, $\upsilon_{C=O\ acylpyz}$).

Synthesis of complex 19

Complex $[Tb(L^5)_3(H_2O)_2]$ (**19**) was prepared using 3 eq HL^5 ligand (3 mmol, 1.0203 g). Yield (%): 91.41% (1.1089 g), M.P.: >200 °C, Formula: $C_{57}H_{52}N_6Cl_3O_8Tb$, Formula wt: 1214.35. Elemental analysis: C, 56.38; H, 4.32; N, 6.92%; Found: C, 57.09; H, 4.578; N, 6.81%. Λ_M = 4.03 $\Omega^{-1}cm^2mol^{-1}$. **FTIR (KBr, cm^{-1}):** 2900-3100 (w, $\upsilon_{O\text{-}H\ water}$), 1616 (s, $\upsilon_{C=O\ DMB}$), 1588 (s, $\upsilon_{C=O\ acylpyz}$).

Synthesis of complex 20

Complex $[Tb(L^6)_3(H_2O)_2]$ (**20**) was prepared using 3 eq HL^6 ligand (3 mmol, 0.96 g). Then the complex was dissolved in a 1:1 ethanol-water mixture to obtain colourless prismatic crystals through recrystallization using the slow evaporation technique. Yield (%): 84.90% (0.9779 g), M.P.: >200 °C, Formula: $C_{60}H_{61}N_6O_8Tb$, Formula wt: 1153.11. Elemental analysis: C, 62.50; H, 5.33; N, 7.29%; Found: C, 61.22; H, 5.371; N, 6.76%. Λ_M = 3.64 $\Omega^{-1}cm^2mol^{-1}$. **FTIR (KBr, cm^{-1}):** 2900-3100 (w, $\upsilon_{O\text{-}H\ water}$), 1620 (s, $\upsilon_{C=O\ PCB}$), 1606 (s, $\upsilon_{C=O\ acylpyz}$).

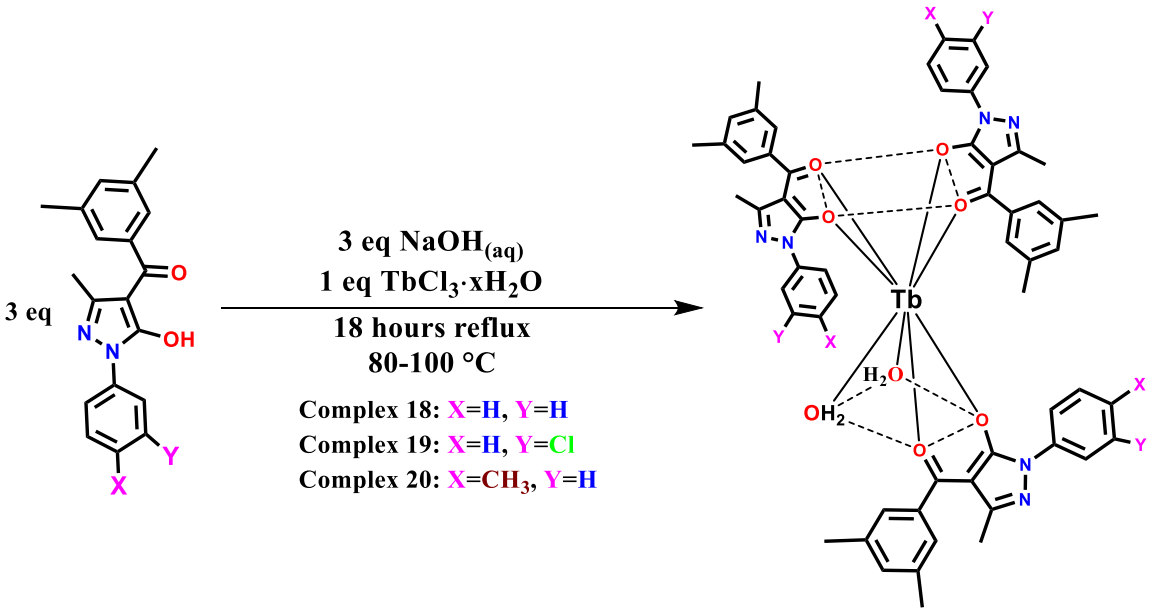

Figure 5.1 Synthetic pathway for complexes 18, 19, and 20.

5.2.3 Physical measurements and characterization techniques

We employed analogous equipment, methods, or software to analyze the statistics of synthesized compounds obtained through FTIR, mass spectrometry, TG-

DTA, and powder XRD, as previously mentioned in Chapter 3(a). All mass spectra were collected via the XEVO G2-XS QTOF at IIT Ropar. Elemental analyses were conducted utilizing an Unicube V1.3.2 (065bdfa) elementar analyzer. Single crystal X-ray data were gathered using an XtaLAB Synergy, Dualflex, HyPix device with a graphite monochromator and Cu-K_α radiation ($\lambda = 1.54178$ Å). The diffraction data were solved, and computations were performed using the SHELXT and SHELXL-2018/3 software packages [25,26].

5.3 Results and Discussion

The structural validation and other spectral characteristics can be comprehended by analyzing the following data of the synthesized terbium complexes. Despite the analysis being conducted on dried samples, the hygroscopic nature of the complexes may cause slight variations in elemental analysis, PXRD, or TGA results. However, these variations do not impact the photophysical properties.

5.3.1 Mass spectral analysis

Mass spectra of complexes 18, 19, and 20 were recorded in methanol/acetonitrile solvent, and its compatibility with the suggested geometry is discussed. The complexes 18, 19, and 20 shows m/z peak of protonated ligand ($[H\text{-}L]^+$) peak at 307.13 ($[C_{19}H_{18}N_2O_2]^+$), 341.09 ($[C_{19}H_{12}ClN_2O_2]^+$), and 321.14 ($[C_{20}H_{19}N_2O_2]^+$), respectively. As all mass spectra were recorded in methanol/acetonitrile solvent, the replacement of two coordinated water molecules from the suggested geometry $[Tb(L)_3(H_2O)_2]$ by methanol and acetonitrile is observed. Therefore, corresponding m/z peaks for geometry $[Tb(L)_3(MeOH)(CH_3CN)]$ are observed at around 1153.25 ($[C_{57}H_{59}N_6O_{10}Tb]^+$) in complex 18, 1255.12 ($[C_{57}H_{56}Cl_3N_6O_{10}Tb]^+$) in complex 19, and 1195.29 ($[C_{60}H_{65}N_6O_{10}Tb]^+$) in complex 20. All mass spectra are provided in Figures 5.2–5.4.

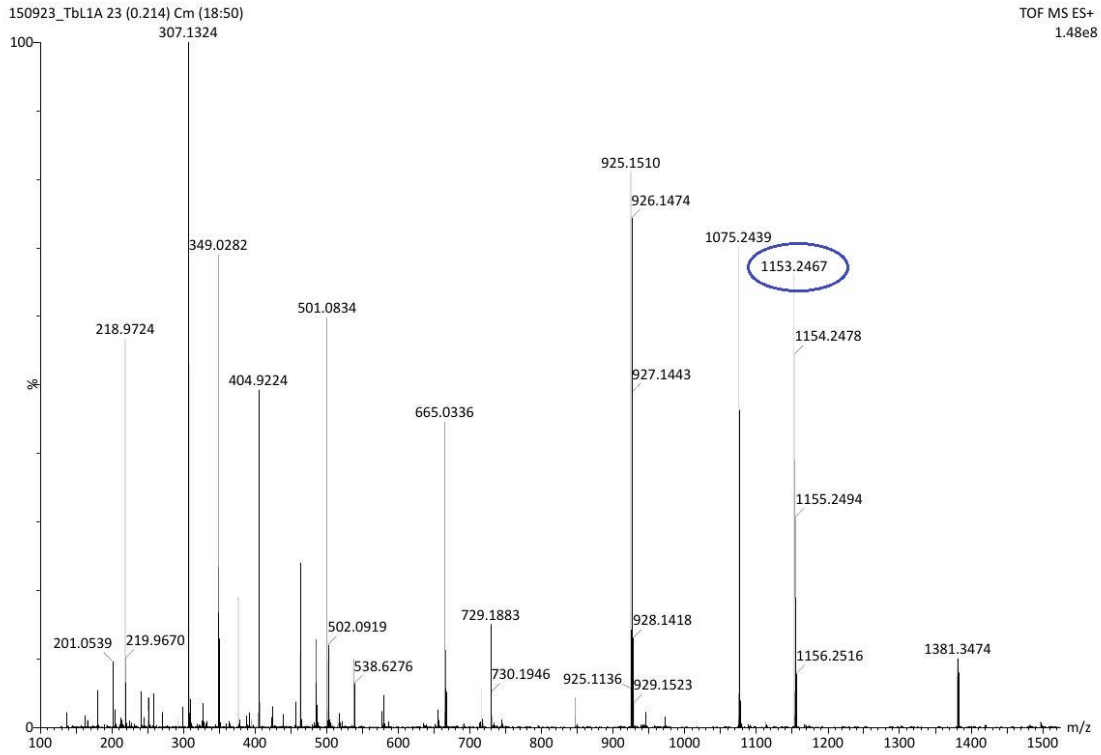

Figure 5.2 Mass spectrum of complex 18.

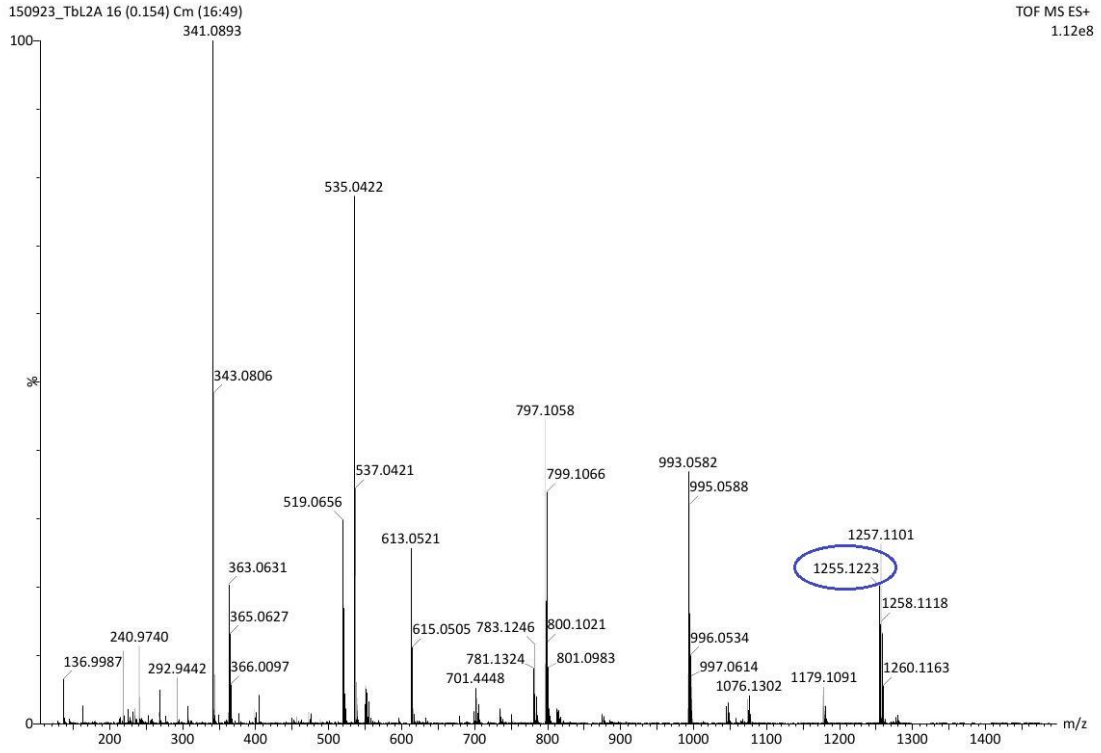

Figure 5.3 Mass spectrum of complex 19.

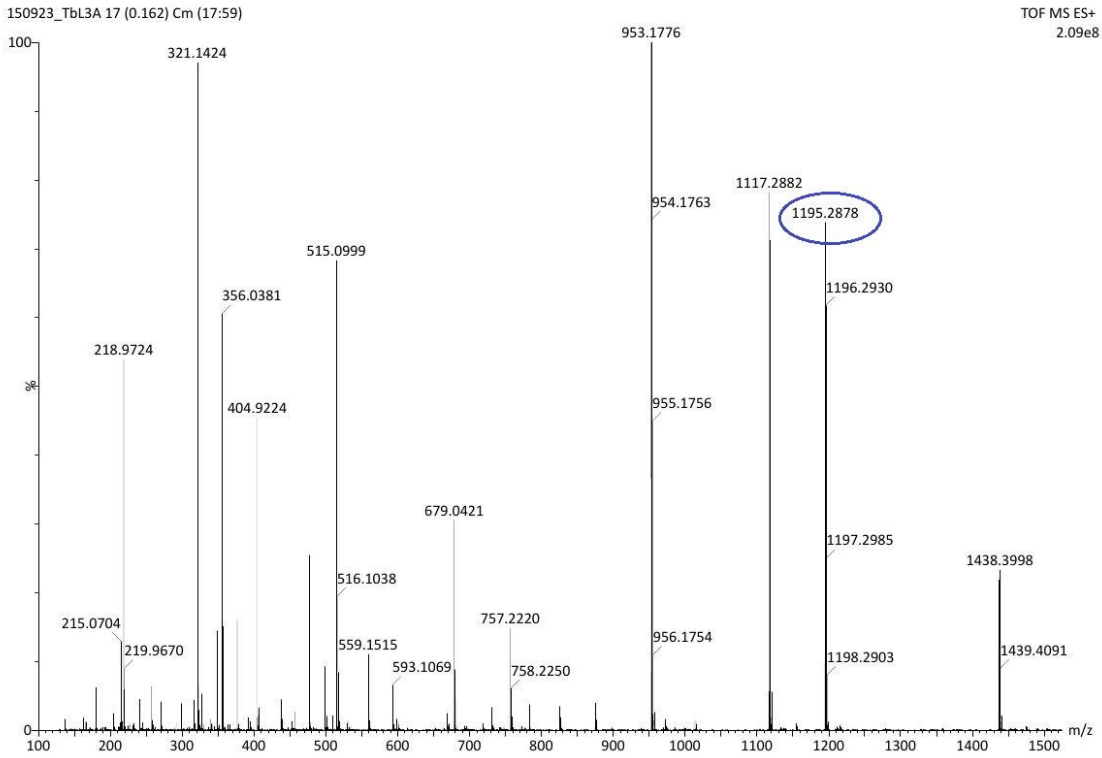

Figure 5.4 Mass spectrum of complex 20.

5.3.2 FTIR spectral analysis

Starting with higher frequency bands, the FTIR bands in the 3100-2900 cm^{-1} range for $\upsilon_{O\text{-}H(water)}$ are observed, indicating the presence of H_2O ligand. As a result of the formation of C=O→Tb bonds, the stretching frequency of $\upsilon_{C=O}$ in the 3,5-dimethyl benzoyl and pyrazolone groups decreases in the complexes compared to their respective ligands (See Table 5.1). The FTIR spectra, depicted in Figures 5.5–5.7, reveal additional bands corresponding to $\upsilon_{C=C}$, $\upsilon_{C=N\ cyclic}$, $\upsilon_{C–H}$, and $\upsilon_{N–N}$, which were assigned to all complexes.

Table 5.1 The FTIR values for terbium complexes (in cm^{-1}).

Vibrations (in cm^{-1})	HL^4 ligand	Complex 18	HL^5 ligand	Complex 19	HL^6 ligand	Complex 20
$\nu_{(O\text{-}H)}$ water	-	2900-3100	-	2900-3100	-	2900-3100
$\nu_{(C=O)}{}^{A}$	1621	1617	1624	1616	1622	1620
$\nu_{(C=O)}{}^{B}$	1605	1596	1589	1588	1607	1601
cyclic $\nu_{(C=N)}$	1511	1492	1554	1480	1511	1494
$\nu_{(C=C)}$	1307	1369	1344	1363	1356	1369
$\nu_{(N\text{-}N)}$	1175	1145	1176	1145	1175	1145
C-H in plane deformation	1067	1072	1080	1071	1066	1064
^{A}dimethyl-benzoyl, ^{B}acyl-pyz						

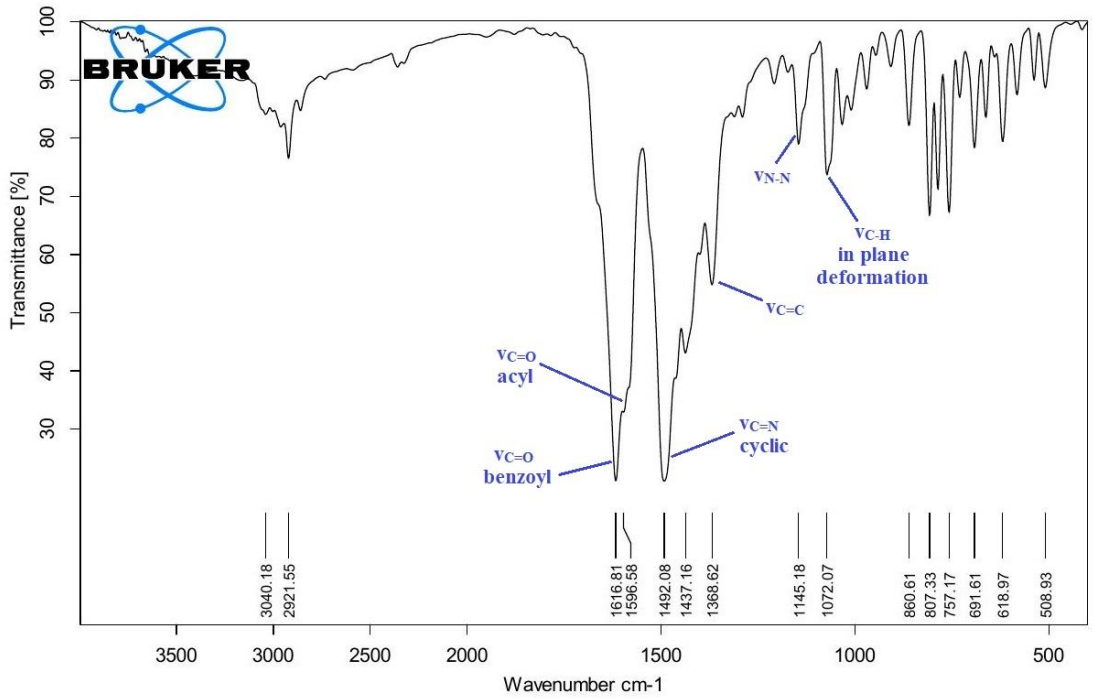

Figure 5.5 FTIR spectrum of complex 18.

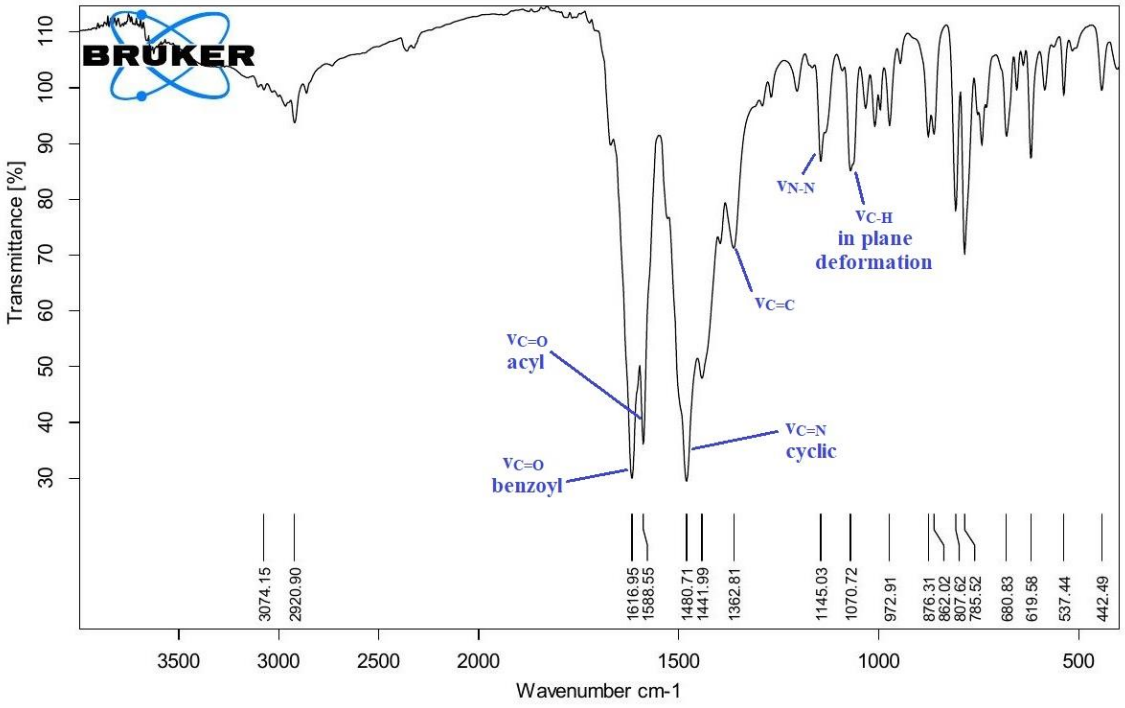

Figure 5.6 FTIR spectrum of complex 19.

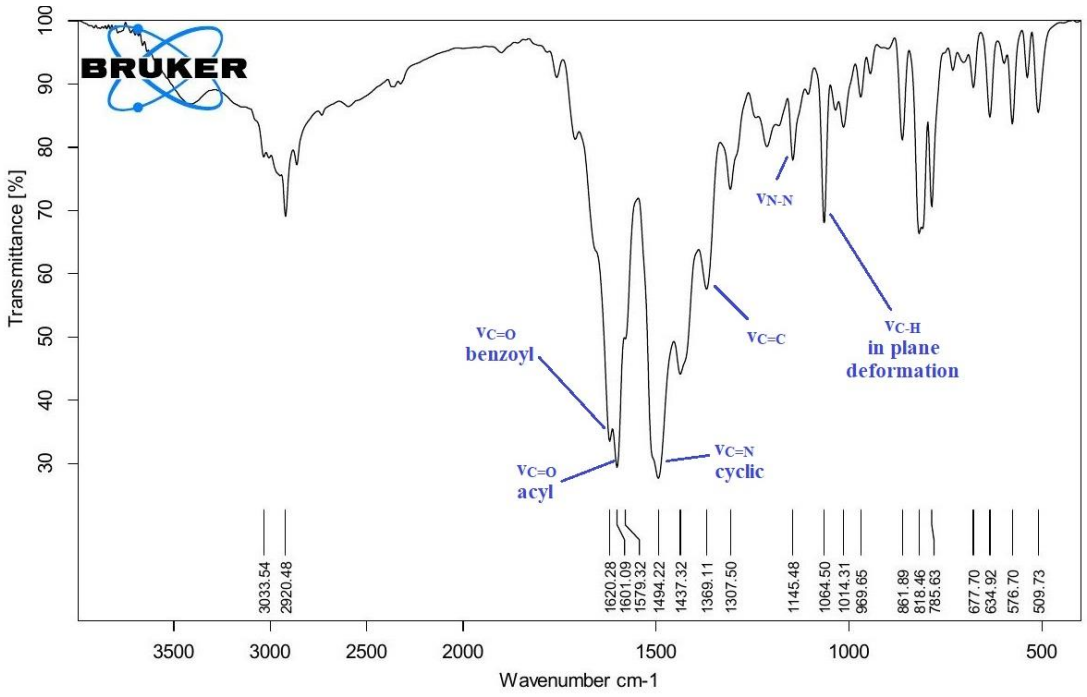

Figure 5.7 FTIR spectrum of complex 20.

5.3.3 Thermogravimetric analysis

The complexes underwent thermal analysis as thermal stability significantly influences their volatility. For the complexes 18, 19, and 20, two degradation steps were observed in the TGA, resulting in overall mass losses of 56.13%, 52.7%, and 58.7%, respectively. Terbium acylpyrazolone complexes are typically hygroscopic [22]. As a result, the initial degradation may include the mass loss of both coordinated and crystalline/hydrated water. The first degradation occurred with mass losses of 12.88% ($8H_2O$), 11.9% ($8H_2O$), and 14.4% ($9H_2O$) in complexes 18, 19, and 20, respectively. Second degradation occurred with mass losses of 43.25%, 40.8%, and 44.3% in complexes 18, 19, and 20, respectively, due to the removal of two ligands. The final thermal decomposition product of the complex is Tb_2O_3. The DTG curves indicate maximum losses of 371.4, 514.2, and 274.7 μg min^{-1} for complexes 18, 19, and 20, respectively, occurring at 413.1, 426.6, and 421.9 °C. The thermogravimetric curves can be found in Figures 5.8–5.10.

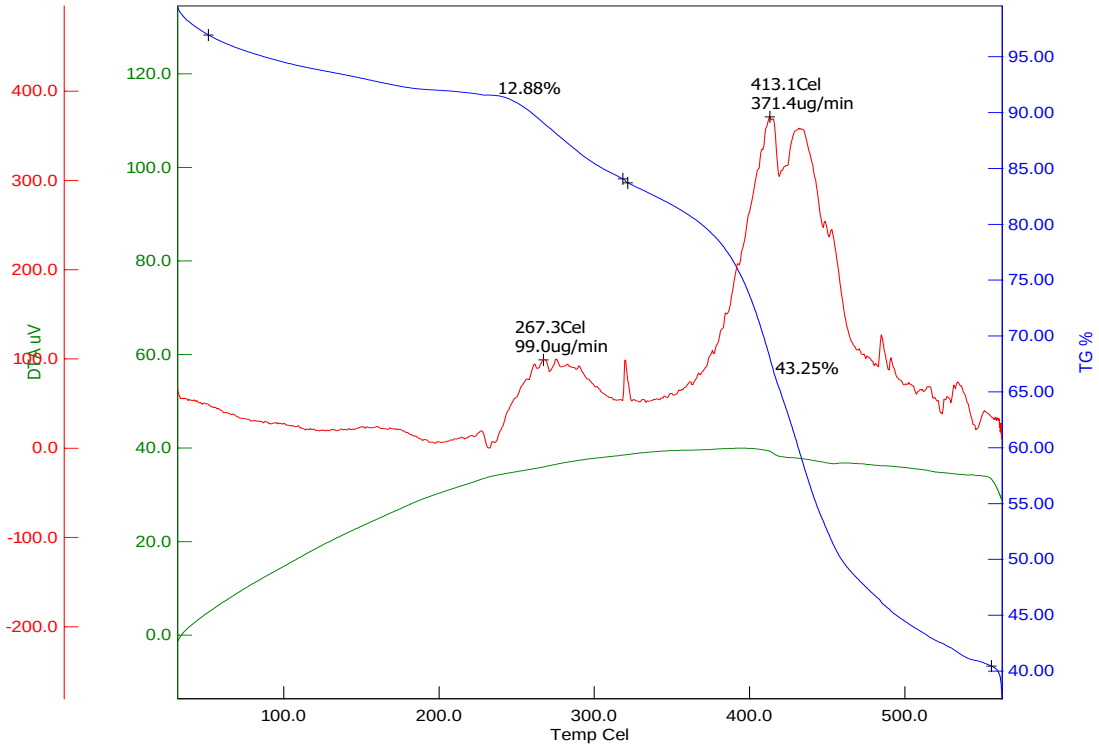

Figure 5.8 Thermogravimetric curve for complex 18.

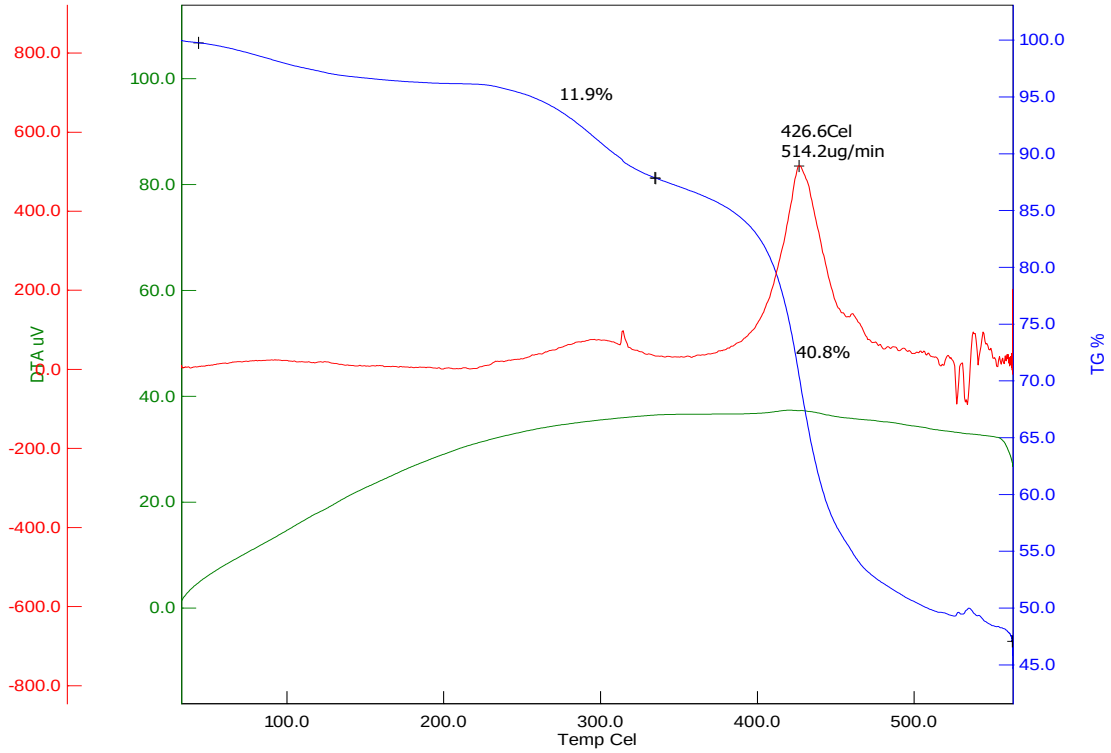

Figure 5.9 Thermogravimetric curve for complex 19.

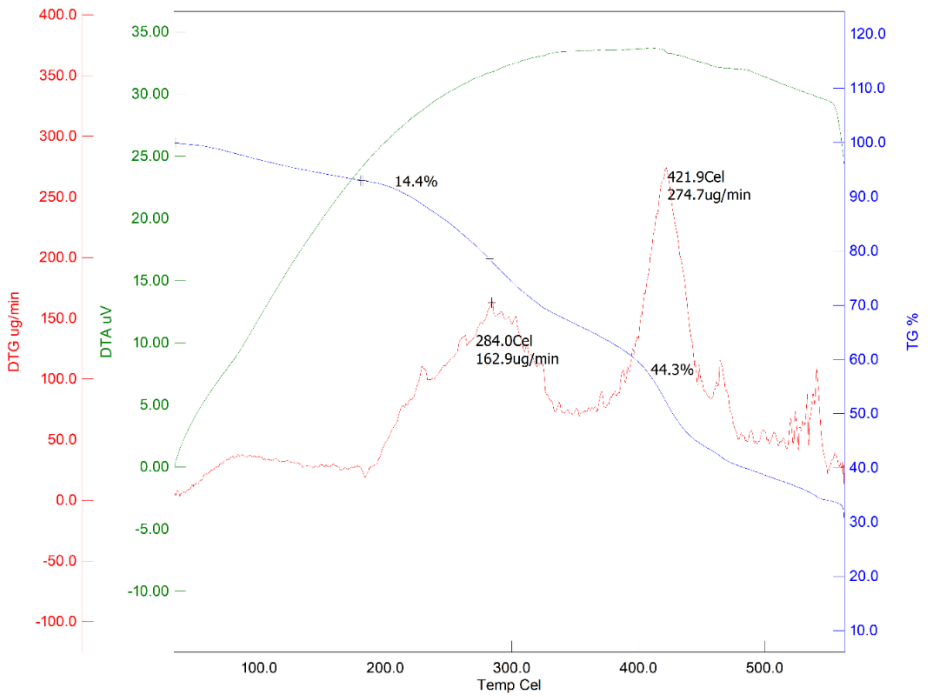

Figure 5.10 Thermogravimetric curve for complex 20.

5.3.4 Single crystal X-ray analysis

Colourless prismatic crystals of complex 20 were obtained through recrystallization in a 1:1 ethanol-water mixture followed by the slow evaporation technique. A mononuclear eight-coordinated bicapped trigonal prismatic polyhedron with the $P\bar{1}$ space group of the triclinic system is formed, wherein six oxygen atoms from the DMBPTMP ligand (O1-O6) and two oxygen atoms from water are bound to the Tb(III) ion, as illustrated in Figures 5.11(a) and 5.11(b). The refinement parameters are presented in Table 5.2. The crystal of complex 20 exhibits the arrangement illustrated in Figure 5.11(c), chosen from among several reported possibilities [24]. Due to the large Tb-Tb distance (8.702 Å), the crystalline material meets the low energy movement criteria [27]. The formation of a six-membered chelating ring occurs due to the binding of terbium with the oxygen atoms of bidentate ligands [28,29].

The twofold axis passes through the midpoint of the O3···O6 and Tb (See Figure 5.11(b)), indicating a strong inclination towards C_{2v} symmetry. All other bond parameters are listed in Table 5.3. Furthermore, the observed loss of planarity in both the upper (O1-O2-O1w) and lower (O4-O5-O2w) faces suggests a slight deviation from bicapped trigonal prismatic geometry.

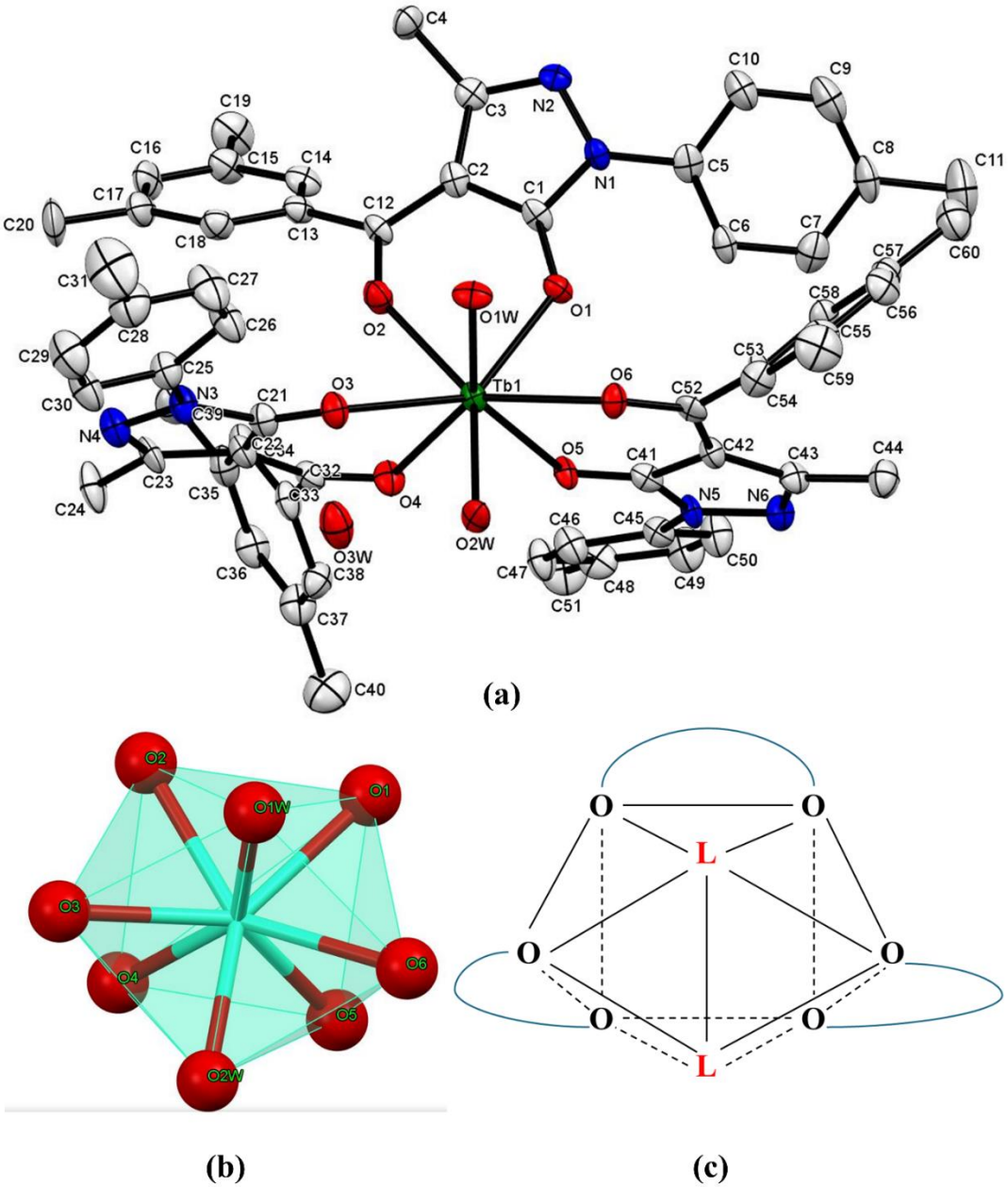

Figure 5.11 (a) Molecular structure of complex 20 with 50% ellipsoid probability, **(b)** coordination polyhedron, and **(c)** bicapped trigonal prismatic arrangement.

The Tb-O binding results in a reduction of the C=O bond order. As a result, the bond lengths of C(32)–O(4) (1.256(7) Å), C(12)–O(2) (1.261(7) Å), and C(52)–O(6) (1.259(7) Å) are observed to be higher than the ideal ketone C=O bond length of 1.23 Å [30]. Table 5.4 elucidates the intermolecular N···H hydrogen bonding between the nitrogen of pyrazolone and the hydrogen of water, as well as the O···H hydrogen bonding between the oxygen atom of external crystalline water and the hydrogen atom of coordinated water.

Table 5.2 Crystallographic structural refinement for complex 20.

Code	Complex 20
Empirical formula	$C_{60}H_{63}N_6O_9Tb$
Formula weight	1171.08
Temperature	100(2) K
Wavelength	1.54184 Å
Crystal system	Triclinic
Space group	$P\bar{1}$
Unit cell dimensions	a = 12.2976(3) Å, b = 15.4969(3) Å, c = 17.4160(4) Å, α = 66.773(2)°, β = 84.886(2)°, γ = 66.706(2)°
Volume	2792.63(12) $Å^3$
Z	2
Density (calculated)	1.393 Mg/m^3
Absorption coefficient	6.726 mm^{-1}
F(000)	1204
Crystal size	0.297 x 0.191 x 0.101 mm^3
Final R indices [I>2sigma(I)]	R_1 = 0.0609, wR_2 = 0.1555
R indices (all data)	R_1 = 0.0745, wR_2 = 0.1834
Theta range for data collection	2.770 to 78.968°
Index ranges	$-12 \le h \le 15$, $-17 \le k \le 19$, $-21 \le l \le 22$
Reflection collected	38288
Independent reflections	11543 [$R_{(int)}$ = 0.0862]
Completeness to theta = 67.679°	99.9 %
Absorption correction	Gaussian
Max. and min. transmission	1.000 and 0.282
Refinement method	Full-matrix least-squares on F^2
Goodness-of-fit on F^2	1.070
Data / restraints / parameters	11543 / 9 / 715
Largest diff. peak and hole	1.603 and -2.881 e.$Å^{-3}$
Empirical formula	$C_{60}H_{63}N_6O_9Tb$

Table 5.3 Selected bond lengths(Å) and bond angles(°) of complex 20.

Bond parameters in complex 20					
Atoms	**Bond lengths**	**Atoms**	**Bond angles**	**Atoms**	**Bond angles**
Tb(1)-O(5)	2.272(4)	O(5)-Tb(1)-O(1)	76.34(14)	O(1)-Tb(1)-O(6)	74.54(13)
Tb(1)-O(2)	2.345(4)	O(2)-Tb(1)-O(1)	72.25(14)	O(3)-Tb(1)-O(6)	127.53(14)
Tb(1)-O(1)	2.348(4)	O(2)-Tb(1)-O(3)	70.10(14)	C(1)-O(1)-Tb(1)	131.4(4)
Tb(1)-O(3)	2.359(4)	O(5)-Tb(1)-O(4)	71.87(14)	C(12)-O(2)-Tb(1)	141.0(4)
Tb(1)-O(4)	2.367(4)	O(2)-Tb(1)-O(4)	74.47(15)	C(21)-O(3)-Tb(1)	126.7(4)
Tb(1)-O(2W)	2.370(4)	O(3)-Tb(1)-O(4)	73.77(14)	C(32)-O(4)-Tb(1)	133.0(4)
Tb(1)-O(1W)	2.437(4)	O(5)-Tb(1)-O(2W)	88.14(14)	C(41)-O(5)-Tb(1)	132.5(4)
Tb(1)-O(6)	2.438(4)	O(3)-Tb(1)-O(2W)	71.68(14)	C(52)-O(6)-Tb(1)	134.0(4)
O(1)-C(1)	1.268(7)	O(4)-Tb(1)-O(2W)	90.42(16)	O(3)-C(21)-N(3)	123.0(5)
O(2)-C(12)	1.261(7)	O(2)-Tb(1)-O(1W)	83.81(15)	O(4)-C(32)-C(22)	123.1(5)
O(3)-C(21)	1.257(7)	O(1)-Tb(1)-O(1W)	83.28(14)	O(4)-C(32)-C(33)	116.8(5)
O(4)-C(32)	1.256(7)	O(3)-Tb(1)-O(1W)	74.53(15)	O(5)-C(41)-C(42)	131.4(5)
O(5)-C(41)	1.249(7)	O(2W)-Tb(1)-O(1W)	90.77(15)	O(6)-C(52)-C(42)	121.7(5)
O(6)-C(52)	1.259(7)	O(5)-Tb(1)-O(6)	73.35(13)	O(6)-C(52)-C(53)	117.2(5)

Table 5.4 Hydrogen bonds for complex 20 [Å and °].

D-H...A	d(D-H)	d(H...A)	d(D...A)	<(DHA)
O(1W)-H(1W1)...N(2)#1	0.84(2)	1.95(3)	2.765(6)	163(7)
O(2W)-H(2W1)...N(6)#2	0.84(2)	1.97(4)	2.731(7)	150(8)
O(2W)-H(2W2)...O(3W)	0.84(2)	1.93(4)	2.685(6)	148(7)
O(3W)-H(3W1)...O(3)	0.86(2)	2.04(6)	2.778(6)	144(9)
O(3W)-H(3W2)...N(4)#3	0.85(2)	2.01(3)	2.854(7)	169(10)

Symmetry transformations used to generate equivalent atoms:

#1 -x+1,-y,-z+1 #2 -x+1,-y+1,-z+1 #3 -x+1,-y+1,-z

A slow evaporation technique obtained bright colourless prismatic crystals of complex 20. Attempts to get x-ray quality crystals of the other two complexes were proved futile. Therefore, a simulated pattern was obtained for complex 20 from the single crystal data, and the same was compared with the pattern obtained experimentally from the powder XRD experiment of complexes 18–20. The simulated pattern of complex 20 matches well with the experimental pattern for all three complexes, as shown in Figure 5.12. This confirms that all the complexes have similar geometry and structure. This also ensures the structure obtained from a single crystal represents the bulk of the complexes. In the XRD graph, a sharp band is observed with maxima in the range 2θ = 5 to 10°, indicating that the complexes are crystalline.

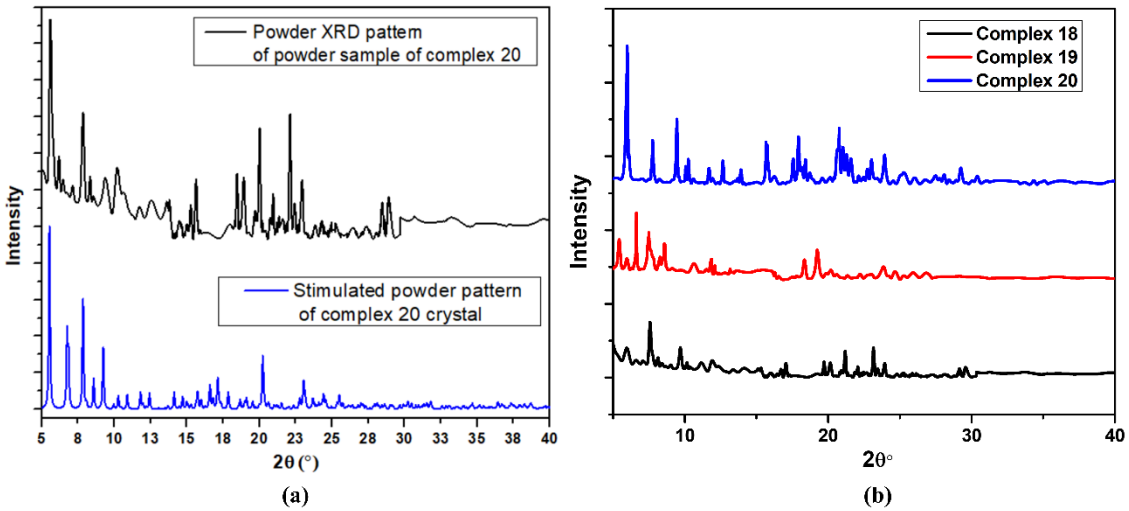

Figure 5.12 (a) Comparison between calculated powder XRD pattern for complex 20 crystal and experimental powder XRD pattern of complex 20, and **(b)** Experimental powder XRD patterns of complexes 18, 19, and 20.

5.3.5 Hirshfeld Surface (HS) analysis

The hydrogen bonding interactions mentioned above can be comprehensively visualized through the d_{norm} Hirshfeld surface analysis conducted using Crystal Explorer 17.5. Closer short interactions are indicated by red dots on d_{norm} HS. The interactions between H(HS)···H(NBs), H(HS)···All(NBs), and All(HS)···H(NBs) on the surface of complex 20 exhibit significant interactions (65.7, 80.0, and 81.9%, respectively) with neighbouring molecules. Additional interactions on different surfaces are depicted in Figure 5.13 within a volume of 1384.81 $Å^3$. π-π stacking interactions contribute to the strength of the crystal lattice, manifesting as a curved portion in the curvedness surface. Figure 5.14 illustrates the visualization of Hirshfeld Percentage interactions in graphical format, achieved by calculating 2D-FP plots depicted in Figure 5.15.

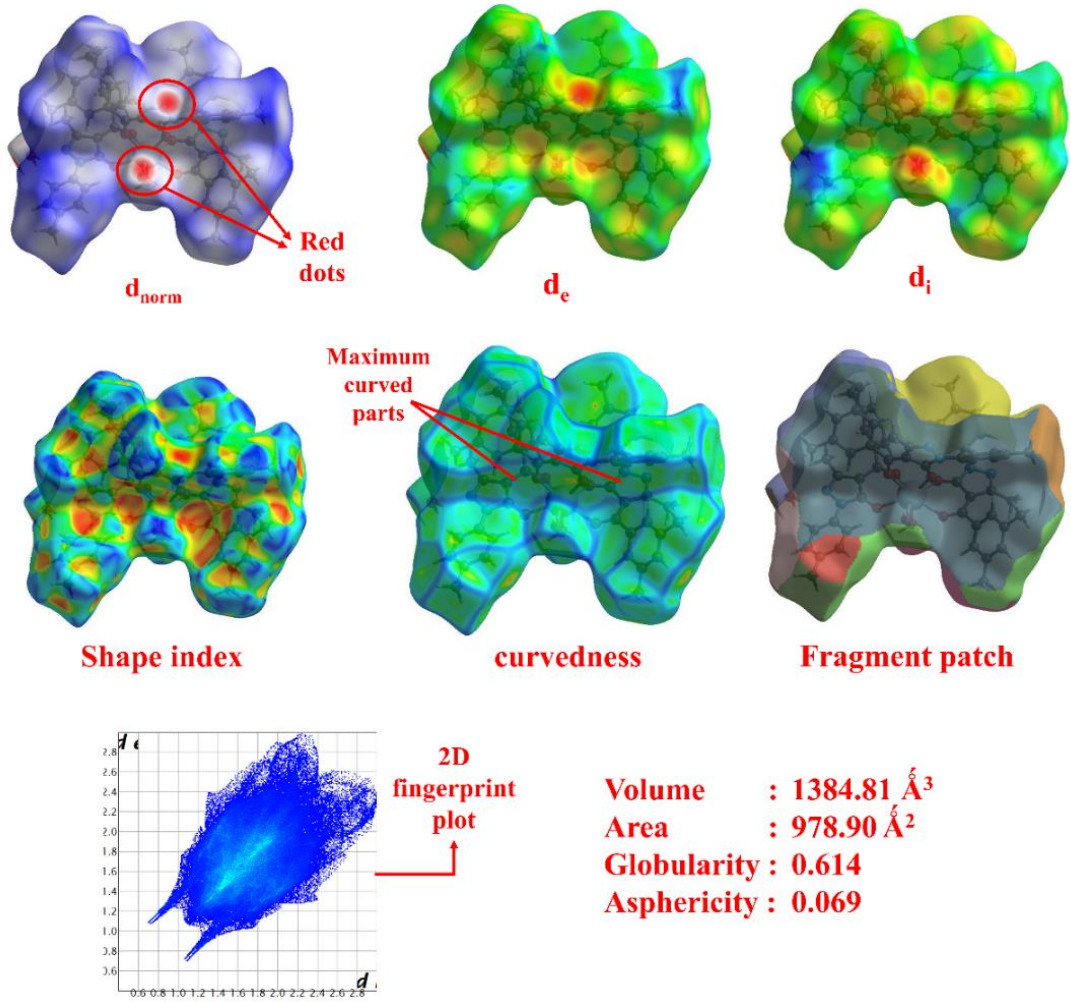

Figure 5.13 Different Hirshfeld surfaces for complex 20.

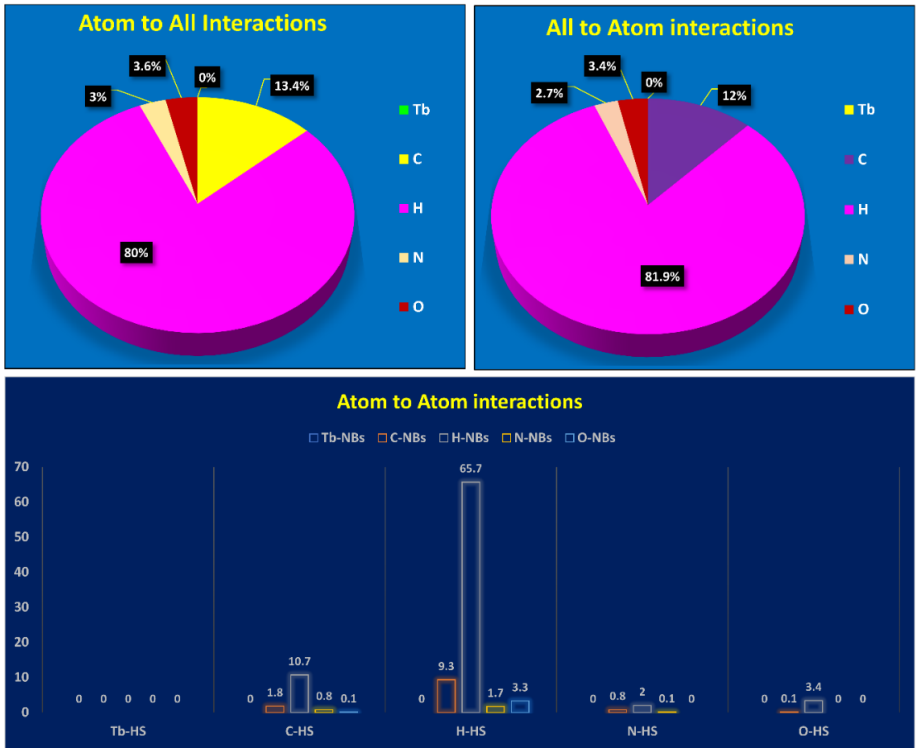

Figure 5.14 Visualization of Hirshfeld Percentage interactions in graphical form.

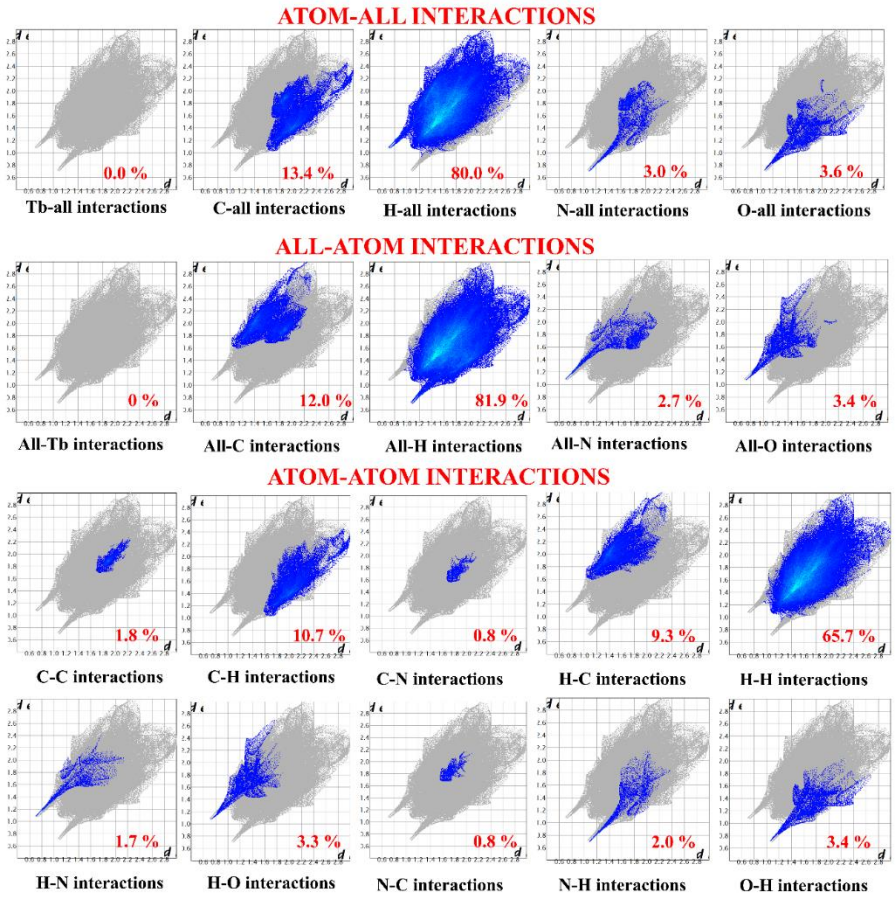

Figure 5.15 Two-dimensional Fingerprint (2D-FP) graphs through Hirshfeld surface analysis of complex 20.

5.3.6 Photophysical analysis

The electronic or UV-Vis spectra in the solid state for all three complexes were acquired and are depicted in Figure 5.16. The spectra of all the complexes exhibit a uniform pattern. The broad and relatively weak 300–450 nm peak results from a ligand-to-metal charge transfer reaction. The peak corresponding to the mentioned transition is identified at approximately 393 nm. Therefore, the solid-state emission spectra of all three complexes were recorded using an excitation wavelength of 393 nm, as illustrated in Figure 5.17.

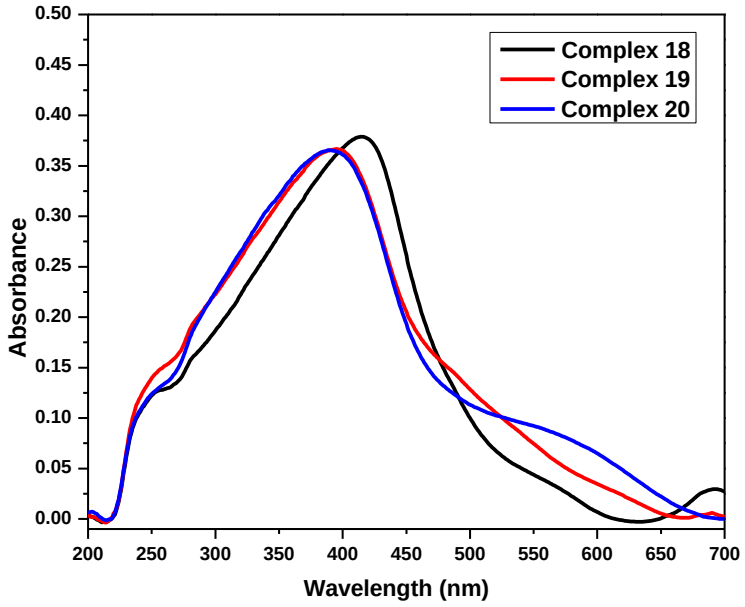

Figure 5.16 Electronic spectra in solid state for complexes 18, 19, and 20.

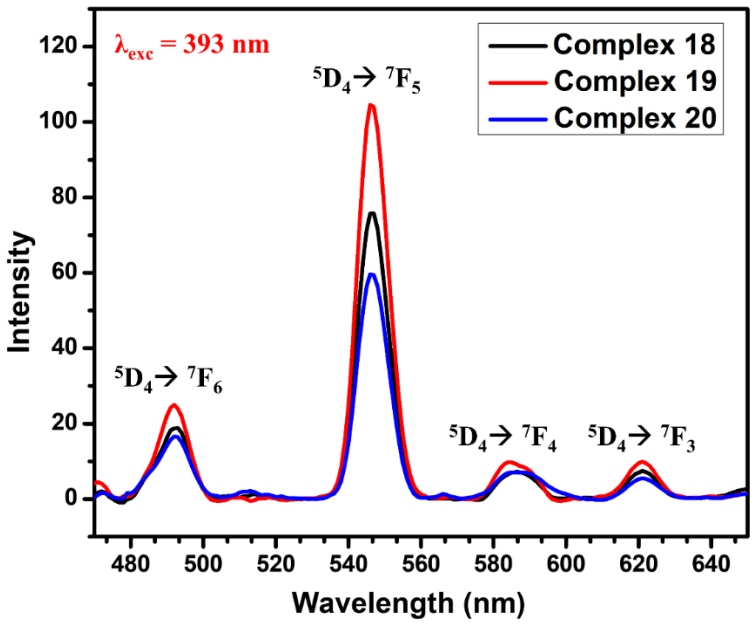

Figure 5.17 Solid-state fluorescence emission spectra for complexes 18, 19, and 20.

The MD transition $^5D_4 \rightarrow {}^7F_6$ is located in the blue spectrum, observed approximately in 480–500 nm. The predominant peak, signifying the transition from $^5D_4 \rightarrow {}^7F_5$, is situated in the green region spanning 540 to 560 nm. A forced ED induces this transition and is notably influenced by the surrounding environment. The heightened intensity of this transition arises from the low symmetric position of Tb^{3+}, caused by the distorted bicapped trigonal prismatic geometry inherent in the complexes. The disparity in intensity between electric dipole (ED) and magnetic dipole (MD) transitions implies a relatively less asymmetric environment [31]. In the case of complexes 18, 19, and 20, the Green-to-Blue (G/B) ratio was determined as 3.70, 4.15, and 3.37, respectively. The G/B ratios, all exceeding unity (G/B > 1), suggest an enhanced level of Tb-O covalency. Remarkably, the luminescence intensity of these three complexes is inferior to that of previously reported complexes. This reduction in intensity within the complexes is attributed to the inclusion of water solvent molecules in the coordination sphere. These water molecules feature high-energy O–H oscillators, which promote non-radiative processes, effectively dampening the luminescence intensity. The transitions from $^5D_4 \rightarrow {}^7F_4$ (580–600 nm) and $^5D_4 \rightarrow {}^7F_3$ (610–630 nm) generate the least intense peaks in the yellow and orange regions, respectively.

The green emission of the complexes is additionally confirmed through the CIE chromaticity colour coordinates (x and y), as depicted in Figure 5.18. The colour coordinates are derived from the emission spectra with excitation at 393 nm, and their respective values are reported as x = 0.305; y = 0.589 for complex 18, x = 0.309; y = 0.602 for complex 19, and x = 0.309; y = 0.565 for complex 20. The percentage of relative green colour purity was determined using the CIE chromaticity colour coordinates for the hypersensitive transition (Table 5.5). The sequence of green colour purity aligns with the order complexes 19 > 18 > 20, precisely corresponding to the G/B ratio order.

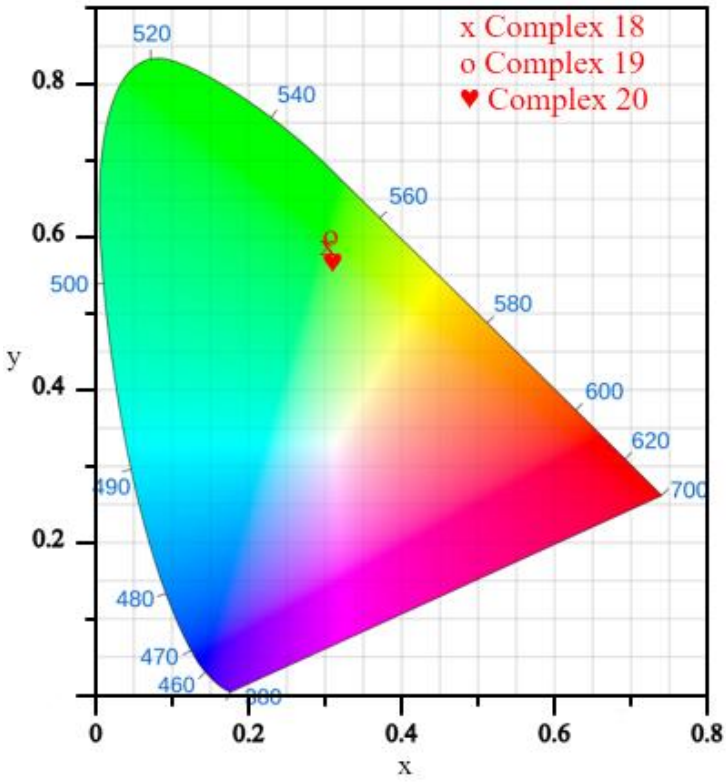

Figure 5.18 The CIE chromaticity diagram for complexes 18, 19, and 20.

Table 5.5 The fluorescence data and relative green colour purity percentage for hypersensitive transition in complexes 18, 19, and 20.

Complex	$\lambda_{exc.}$ (nm)	$\lambda_{em.}$ (nm)	Transitions assignments	Colour purity (%)
18	393	492.5	$^5D_4 \rightarrow {}^7F_6$	68.74
		546.5	$^5D_4 \rightarrow {}^7F_5$	
		586.3	$^5D_4 \rightarrow {}^7F_4$	
		621.0	$^5D_4 \rightarrow {}^7F_3$	
19	393	492.5	$^5D_4 \rightarrow {}^7F_6$	70.83
		546.4	$^5D_4 \rightarrow {}^7F_5$	
		586.3	$^5D_4 \rightarrow {}^7F_4$	
		621.0	$^5D_4 \rightarrow {}^7F_3$	
20	393	491.8	$^5D_4 \rightarrow {}^7F_6$	62.68
		546.5	$^5D_4 \rightarrow {}^7F_5$	
		584.5	$^5D_4 \rightarrow {}^7F_4$	
		621.1	$^5D_4 \rightarrow {}^7F_3$	

Figure 5.19 depicts the energy absorption process by the acylpyrazolones, recognized as the "CL (central ligand)." The absorbed energy is then transferred to the metal ion and returns to the ground state. This diagram helps elucidate the emission process of terbium ions. The central ligand undergoes energy absorption, transitioning to its singlet state and intersystem crossing to its triplet state. Subsequently, the energy is intramolecularly transferred to the energy levels of the Tb(III) ion. The concept of enhancing stability through absorption, fluorescence, and charge transfer can be more thoroughly understood using the light energy conversion diagram known as the "antenna effect."

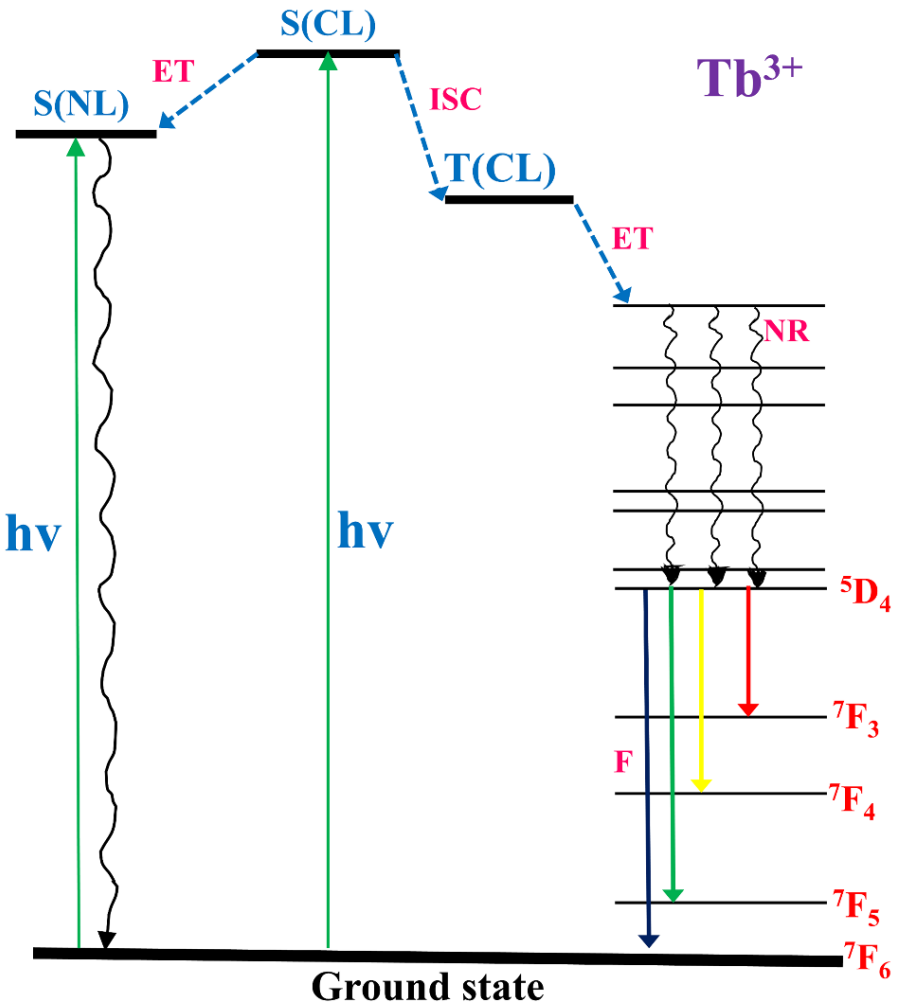

Energy level diagram for Tb^{3+} complex, where CL = central ligand, NL = neutral ligand, S = singlet excited state, T = triplet excited state, ET = intramolecular energy transfer, ISC = intersystem crossing, F = Fluorescence decay, NR = Non-radiative pathway

Figure 5.19 "Antenna effect" diagram showing the mechanism of the emission process in Terbium-acylpyrazolone complexes.

5.4 Conclusions

The main aims of this study were to explore the fluorescence peaks of Tb(III)-acylpyrazolone complexes and to examine how structural variations among ligands in different complexes affect the G/B ratio, showcasing the purity of green emission. Three mononuclear eight-coordinated bicapped trigonal prismatic terbium complexes 18, 19 and 20 were synthesized, wherein six oxygen atoms from the L^6 ligand (O1-O6) and two oxygen atoms from water are bound to the Tb(III) ion. The structures of these complexes were comprehensively analyzed using ESI mass, FT-IR, UV-Vis, powder XRD, and TG-DTA methods. The solid-state emission spectra were analyzed to identify four transitions, categorize their types, and determine the G/B ratio corresponding to different regions. The G/B ratio surpasses unity (G/B > 1), signifying an elevated level of Tb-O covalency. The confirmation of green emission from the complexes is further validated using the CIE chromaticity diagram. The intensity of solid-state emission spectra was comprehensively examined using their antenna effect energy diagram. The research demonstrated the potential to modify the chemical and spectroscopic properties of acylpyrazolone to synthesize multi-dentate Tb(III) complexes. These complexes appeal to various applications, including material sensing and scanning, potentially contributing to understanding biological mechanisms or diagnosing diseases.

References

[1] S. Pramanik, A. Kumari, M.K. Sinha, B. Munshi, S.K. Sahu, Valorization of phosphor powder of waste fluorescent tubes with an emphasis on the recovery of terbium oxide (Tb_4O_7), Sep Purif Technol 322 (2023) 124332. https://doi.org/10.1016/j.seppur.2023.124332.

[2] E. Girotto, A. Pereira, C. Arantes, M. Cremona, A.J. Bortoluzzi, C.A.M. Salla, I.H. Bechtold, H. Gallardo, Efficient terbium complex based on a novel pyrazolone derivative ligand used in solution-processed OLEDs, J Lumin 208 (2019) 57–62. https://doi.org/10.1016/j.jlumin.2018.12.027.

[3] L. Ajili, A. Selmi, A. Bourezgui, A. Elboughdiri, H. Rahmouni, N. Sdiri, R. Mnaseri, M. Férid, K. Horchani−Naifer, Synthesis and luminescence properties of terbium-doped $AgLa(PO_3)_4$ green light emitting phosphor, Emergent Mater 6 (2023) 1059–1069. https://doi.org/10.1007/s42247-023-00500-4.

[4] R.F. Cavaier, F. Haddad, T. Sounalet, T. Stora, I. Zahi, Terbium Radionuclides for Theranostics Applications: A Focus On MEDICIS-PROMED, Phys Procedia 90 (2017) 157–163. https://doi.org/10.1016/j.phpro.2017.09.053.

[5] J. Chen, M.K. Siddiqui, M. Hussain, N. Hussain, S.M. Eldin, M. Cancan, On characterization of physical properties for terbium (IV) oxide system via curve fitting models, J Mol Struct 1287 (2023) 135560. https://doi.org/10.1016/j.molstruc.2023.135560.

[6] N.T. Rice, I.A. Popov, D.R. Russo, J. Bacsa, E.R. Batista, P. Yang, J. Telser, H.S. La Pierre, Design, Isolation, and Spectroscopic Analysis of a Tetravalent Terbium Complex, J Am Chem Soc 141 (2019) 13222–13233. https://doi.org/10.1021/jacs.9b06622.

[7] J. Yuan, G. Wang, K. Majima, K. Matsumoto, Synthesis of a Terbium Fluorescent Chelate and Its Application to Time-Resolved Fluoroimmunoassay, Anal Chem 73 (2001) 1869–1876. https://doi.org/10.1021/ac0013305.

[8] G. Wakefield, H.A. Keron, P.J. Dobson, J.L. Hutchison, Structural and optical properties of terbium oxide nanoparticles, J Phys Chem Sol 60 (1999) 503–508. https://doi.org/10.1016/S0022-3697(98)00307-2.

[9] ManjuBala, S. Kumar, S. Chahar, V.B. Taxak, P. Boora, S.P. Khatkar, Synthesis, NMR and optical features of intense green color terbium(III) complexes, Optik (Stuttg) 202 (2020) 163636. https://doi.org/10.1016/j.ijleo.2019.163636.

[10] T. Gregório, J. de M. Leão, G.A. Barbosa, J. de L. Ramos, S. Om Kumar Giese, M. Briganti, P.C. Rodrigues, E.L. de Sá, E.R. Viana, D.L. Hughes, L.D. Carlos, R.A.S. Ferreira, A.G. Macedo, G.G. Nunes, J.F. Soares, Promoting a Significant Increase in the Photoluminescence Quantum Yield of Terbium(III) Complexes by Ligand Modification, Inorg Chem 58 (2019) 12099–12111. https://doi.org/10.1021/acs.inorgchem.9b01397.

[11] F. Zhao, X.-Z. Wang, S.-T. He, P.-Z. Ma, W. Zhang, Y.-C. Ma, S.-J. Zhao, J. Sun, Highly sensitive bifunctional sensor of a dinuclear terbium complex, Sens Actuators B Chem 270 (2018) 452–458. https://doi.org/10.1016/j.snb.2018.05.073.

[12] E. Mohammadian, E. Rahimpour, M. Alizadeh-Sani, A. Foroumadi, A. Jouyban, An overview on terbium sensitized based-optical sensors/nanosensors for determination of pharmaceuticals, Appl Spectrosc Rev 57 (2022) 39–76. https://doi.org/10.1080/05704928.2020.1843174.

[13] N. Hildebrandt, K.D. Wegner, W.R. Algar, Luminescent terbium complexes: Superior Förster resonance energy transfer donors for flexible and sensitive multiplexed biosensing, Coord Chem Rev 273–274 (2014) 125–138. https://doi.org/10.1016/j.ccr.2014.01.020.

[14] D.D. Viet, M. Johar, H.N. Khan, Y. Segura-Ramírez, Synthesis and characterization of europium (III), terbium (III) complexes and their mixture for making white light emission powder, Emergent Scientist 7 (2023) 3. https://doi.org/10.1051/emsci/2023003.

[15] N. Sun, X. Zhao, Y. Yang, L. Li, A. Zhang, H. Jia, X. Liu, Synthesis and luminescent properties of terbium complex containing 4-benzoylbenzoic acid for application in NUV-based LED, Journal of Rare Earths 34 (2016) 130–136. https://doi.org/10.1016/S1002-0721(16)60004-2.

[16] A. Hooda, D. Singh, K. Nehra, A. Dalal, S. Kumar, R.S. Malik, B. Rathi, P. Kumar, Luminescent Tb(III) complexes with Lewis bases for displays: Synthesis and spectral

investigation, Inorg Chem Commun 151 (2023) 110583. https://doi.org/10.1016/j.inoche.2023.110583.

[17] E. Rezende Souza, I.G.N. Silva, E.E.S. Teotonio, M.C.F.C. Felinto, H.F. Brito, Optical properties of red, green and blue emitting rare earth benzenetricarboxylate compounds, J Lumin 130 (2010) 283–291. https://doi.org/10.1016/j.jlumin.2009.09.004.

[18] C. Caro, J.M. Paez-Muñoz, A.M. Beltrán, M. Pernia Leal, M.L. García-Martín, PEGylated Terbium-Based Nanorods as Multimodal Bioimaging Contrast Agents, ACS Appl Nano Mater 4 (2021) 4199–4207. https://doi.org/10.1021/acsanm.1c00569.

[19] A. Dalal, K. Nehra, A. Hooda, S. Singh, D. Singh, S. Kumar, Synthesis, Optoelectronic and Photoluminescent Characterizations of Green Luminous Heteroleptic Ternary Terbium Complexes, J Fluoresc 32 (2022) 1019–1029. https://doi.org/10.1007/s10895-022-02920-7.

[20] A. Hooda, K. Nehra, A. Dalal, S. Singh, R. Kumar Saini, S. Kumar, D. Singh, Terbium complexes of an asymmetric β-diketone: Preparation, photophysical and thermal investigation, Inorganica Chim Acta 536 (2022) 120881. https://doi.org/10.1016/j.ica.2022.120881.

[21] F. Liao, Y. Zhang, J. Hu, Enhancement of green emission from $Ca_{14}Al_{10}Zn_6O_{35}$: Tb^{3+} phosphors via cross-relaxation energy transfer by Li^+ ions, J Lumin 231 (2021) 117791. https://doi.org/10.1016/j.jlumin.2020.117791.

[22] F. Marchetti, C. Pettinari, R. Pettinari, Acylpyrazolone ligands: Synthesis, structures, metal coordination chemistry and applications, Coord Chem Rev 249 (2005) 2909–2945. https://doi.org/10.1016/j.ccr.2005.03.013.

[23] F. Marchetti, C. Pettinari, C. Di Nicola, A. Tombesi, R. Pettinari, Coordination chemistry of pyrazolone-based ligands and applications of their metal complexes, Coord Chem Rev 401 (2019) 213069. https://doi.org/10.1016/j.ccr.2019.213069.

[24] F. Marchetti, R. Pettinari, C. Pettinari, Recent advances in acylpyrazolone metal complexes and their potential applications, Coord Chem Rev 303 (2015) 1–31. https://doi.org/10.1016/j.ccr.2015.05.003.

[25] G.M. Sheldrick, Crystal structure refinement with SHELXL, Acta Crystallogr C 71 (2015) 3–8. https://doi.org/10.1107/S2053229614024218.

[26] G.M. Sheldrick, SHELXT – Integrated space-group and crystal-structure determination, Acta Crystallogr A 71 (2015) 3–8. https://doi.org/10.1107/S2053273314026370.

[27] V.F. Shul'gin, S. V Abkhairova, O. V Konnik, S.B. Meshkova, Z.M. Topilova, E.B. Rusanov, G.G. Aleksandrov, I.L. Eremenko, Anionic lanthanide complexes with 3-methyl-4-formyl-1-phenyl-5-pyrazolone, Russ J Inorg Chem 58 (2013) 678–683. https://doi.org/10.1134/S0036023613060223.

[28] L. Shen, M. Shi, F. Li, D. Zhang, X. Li, E. Shi, T. Yi, Y. Du, C. Huang, Polyaryl Ether Dendrimer with a 4-Phenylacetyl-5-pyrazolone-based Terbium(III) Complex as Core: Synthesis and Photopysical Properties, Inorg Chem 45 (2006) 6188–6197. https://doi.org/10.1021/ic052148v.

[29] X.-L. Li, X. Niu, L.-F. He, X.-L. Feng, S.-M. Fang, L.-F. Han, L.-M. Zhou, H.-P. Xiao, Acylpyrazolonate-based lanthanide complexes: Synthesis, crystal structures and photoluminescence properties, Synth Met 161 (2011) 1063–1067. https://doi.org/10.1016/j.synthmet.2011.03.016.

[30] W. and M.J. and S.S. and S.M. and Z.C. Keese R. and Luef, Planarizing Distortions in Polycyclic Carbon Compounds, in: S. de Meijere Armin and Blechert (Ed.), Strain and Its Implications in Organic Chemistry: Organic Stress and Reactivity, Springer Netherlands, Dordrecht, (1989) 283–296. https://doi.org/10.1007/978-94-009-0929-8_20.

[31] A. Ichoja, S. Hashim, S.K. Ghoshal, I.H. Hashim, Absorption and luminescence spectral analysis of Dy^{3+}-doped magnesium borate glass, Chinese Journal of Physics 66 (2020) 307–317. https://doi.org/10.1016/j.cjph.2020.03.029.